Asian Journal of Pharmaceutical Sciences 17 (2022) 253–267

Available online at www.sciencedirect.com

ScienceDirect

journal homepage: www.elsevier.com/locate/AJPS

Original Research Paper

Enhanced photodynamic therapy/photothermo therapy for nasopharyngeal carcinoma *via* a tumour microenvironment-responsive self-oxygenated drug delivery system

Nan Wu[a,1], *Yaqin Tu*[a,1], *Guorun Fan*[a,1], *Jiahui Ding*[b], *Jun Luo*[c], *Wei Wang*[d,*], *Chong Zhang*[b], *Caiyan Yuan*[b], *Handan Zhang*[b], *Pei Chen*[d], *Songwei Tan*[b], *Hongjun Xiao*[a,*]

[a] *Department of Otorhinolaryngology, Union Hospital, Tongji Medical College, Huazhong University of Science and Technology, Wuhan 430022, China*

[b] *School of Pharmacy, Tongji Medical College, Huazhong University of Science and Technology, Wuhan 430030, China*

[c] *Zhejiang Fenghong New Material Co. Ltd., Huzhou 313300, China*

[d] *State Key Laboratory of Materials Processing and Die and Mould Technology, School of Materials Science and Engineering, Huazhong University of Science and Technology, Wuhan 430074, China*

ARTICLE INFO

Article history:
Received 8 November 2021
Revised 27 December 2021
Accepted 23 January 2022
Available online 25 February 2022

Keywords:
Liposome
ICG
Photodynamic therapy
Hypoxia
Tumour therapy

ABSTRACT

The hypoxic nature of tumours limits the efficiency of oxygen-dependent photodynamic therapy (PDT). Hence, in this study, indocyanine green (ICG)-loaded lipid-coated zinc peroxide (ZnO_2) nanoparticles (ZnO_2@Lip-ICG) was constructed to realize tumour microenvironment (TME)-responsive self-oxygen supply. Near infrared light irradiation (808 nm), the lipid outer layer of ICG acquires sufficient energy to produce heat, thereby elevating the localised temperature, which results in accelerated ZnO_2 release and apoptosis of tumour cells. The ZnO_2 rapidly generates O_2 in the TME (pH 6.5), which alleviates tumour hypoxia and then enhances the PDT effect of ICG. These results demonstrate that ZnO_2@Lip-ICG NPs display good oxygen self-supported properties and outstanding PDT/PTT characteristics, and thus, achieve good tumour proliferation suppression.

1. Introduction

Nasopharyngeal carcinoma (NPC) is highly prevalent in South China and seriously affects the quality of human health [1–3]. The annual incidence of NPC is estimated to approach 20–50 new cases per 100 000 individuals, ranking the highest amongst all head and neck cancers [4]. The current therapies for NPC primarily include chemotherapy and radiotherapy

* Corresponding authors.
E-mail addresses: weiwang@hust.edu.cn (W. Wang), xhjent_whxh@hust.edu.cn (H.J. Xiao).
[1] These authors contributed equally to this work.
Peer review under responsibility of Shenyang Pharmaceutical University.

https://doi.org/10.1016/j.ajps.2022.01.002

[5–7]. Traditional cancer therapy has many limitations, including unsatisfactory bioavailability, drug resistance, and side effects such as myelosuppression, gastrointestinal reactions and auditory neurotoxicity. Notably, photodynamic therapy (PDT), as a highly efficacious alternative or supplement to routine cancer treatment, has several unique advantages, including non-invasiveness, remote spatiotemporal control and facile application [8–10]. It uses light-activated photosensitisers to generate reactive oxygen species (ROS) under infrared light irradiation at a specific wavelength, thereby causing irreversible damage to tumour cells [11–14]. However, most of the available photosensitisers are limited by target deficiency, short half-life ($T_{1/2}$), easy aggregation and fluorescence self-quenching. These limitations seriously restrict the clinical application of phototherapy for cancer [11,15,16].

FDA-approved indocyanine green (ICG) is employed in various biomedical applications, including cardiac output measurement [17,18], monitoring of liver and kidney function [19–21], and visceral surgery [22]. More importantly, ICG is well recognised as a photosensitiser and photothermal agent. It exhibits PDT and photothermal therapy (PTT) properties under near infrared (NIR) laser irradiation [23–27]. In view of this, ICG is considered to be one of the most efficacious drugs for cancer management. However, free ICG strongly interacts with plasma proteins in the blood and is rapidly cleared by the liver [28,29]. It also has several intrinsic shortcomings, including concentration-dependent aggregation, easy biodegradation, photo instability and a lack of tumour target specificity, limiting the further biomedical application of ICG [30]. To address these limitations, researchers have developed various methods to deliver ICG, including polymeric nanoparticles, liposomes, lipid-polymer nanoparticles, inorganic particles, carbon nanomaterials, bioconjugates and other formulations [31–36]. Amongst these, liposomes are a commonly used strategy for ICG delivery [37,38]. Thus, in this study, the intention was to add ICG to liposomes. Liposomes can circulate in the bloodstream for an extended period of time and can target tumour via enhanced permeability and retention (EPR) effect [39]. ICG can be physically integrated into the liposome membrane, preventing it from binding to plasma proteins and reducing the occurrence of fluorescence self-quenching. Thus, the combination of ICG and liposomes can improve the tumour targeting specificity of ICG, thereby greatly improving its stability and PTT/PDT efficiency.

It is worth mentioning that the therapeutic effect of ICG is usually limited to the hypoxic feature of most solid tumours, due to the oxygen-dependent nature of photodynamic therapy [40–42]. Many strategies that increase the oxygen supply, with the help of specifically designed oxygen delivery vehicles, have been investigated to improve the PDT effect, including the Fenton reaction, hydrogen peroxide, and haemoglobin, amongst others [43–45]. Recently, metal peroxide (*e.g.*, MgO_2, CaO_2, ZnO_2)-based nanoplatform has been reported to generate O_2 and ROS in cancer cells for molecular dynamic therapy [46,47]. However, MgO_2 and CaO_2 are highly reactive and rapidly decomposes even in the physiological environment (pH = 7.4), triggering the degradation of organic molecules, which limited their application as drug carrier. Compared to MgO_2 and CaO_2, zinc peroxide (ZnO_2) is more stable at neutral pH but decomposes to H_2O_2 and Zn^{2+} at a mildly acidic pH. Thus, it is quite suitable for adoption as an O_2 generation platform combined with ICG to achieve high efficient PDT treatment of tumour [48].

In this study, a novel tumour microenvironment (TME)-responsive self-oxygenated drug delivery system based on ZnO_2 nanoparticles (NPs) coated with ICG-loaded liposomes (denoted as ZnO_2@Lip-ICG) was constructed. As shown in Scheme 1, the ICG in the outer layer of the lipid gains sufficient energy to generate heat upon NIR light irradiation (808 nm), which raises the local temperature and releases ZnO_2 from the liposomes. The ZnO_2 NPs are stable under physiological conditions but highly reactive in a mildly acidic environment. ZnO_2 rapidly generates O_2 in the TME (rich in H^+), which alleviates tumour hypoxia. Meanwhile, the O_2 produced by ZnO_2 is further used by ICG, which "continuously" generates singlet oxygen under NIR irradiation to improve the efficacy of PDT. In cooperation with the PTT property of ICG, ZnO_2@Lip-ICG could induce the apoptosis of tumour cells and thus achieve notable tumour suppression *in vivo*.

2. Materials and methods

2.1. Materials

Cholesterol (Chol), soy lecithin, distearoyl-phosphatidyl-ethanolamine (DSPE-PEG2000), 1, 3-diphenylisobenzofuran (DPBF) and ICG were acquired from Sigma-Aldrich Inc. Foetal bovine serum (FBS), high-glucose DMEM and 0.25% Trypsin EDTA were acquired from Gibco Life Technologies (AG, USA). Penicillin-streptomycin was obtained from Hyclone (USA). DAPI, Calcein-AM/PI double staining kit, RIPA lysis buffer and Cell counting kit-8 were acquired from Beyotime Biotechnology (China). Lysotracker Green was purchased from KeyGEN BioTech (China).Singlet Oxygen Sensor Green (SOSG) was obtained from Invitrogen (NY, USA). The ROS detection kit (DCFH-DA) was purchased from Solarbio Life Science (China). Caspase-3 antibody, Caspase-9 antibody, Caspase-12 antibody and Bax antibody were purchased from Proteintech. Various antibodies, including β-Actin, HSP 90, HIF-1α and TUNEL were acquired from Servicebio. All animal protocols were performed at the Huazhong University of Science and Technology. Four-week-old female nude mice and Sprague Dawley (SD) rats (250 g) were purchased from Wuhan SHULAIBAO Biological Technology Co., Ltd. (China). They were maintained at the Laboratory Animal Centre of the Huazhong University of Science and Technology with standard access to water and food. Animal experiments were approved by the Experimental Animal Ethics Committee of Tongji Medical College of Huazhong University of Science and Technology (IACUC Number: 2510). The nude mice were treated with CNE-2 cells to construct CNE-2 tumour-bearing mice. Animals were sacrificed for further analysis once a tumour maximum diameter of 20 mm was reached.

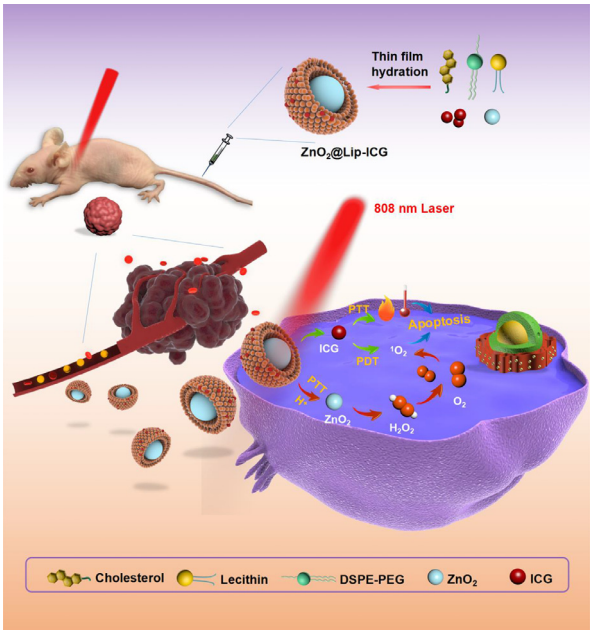

Scheme 1 – Synthesis process of ZnO_2@Lip-ICG nanoparticles and the schematic illustration of TME responsive self-oxygenated drug delivery system (ZnO_2@Lip-ICG NPs) for enhanced PDT of nasopharyngeal carcinoma.

2.2. *Preparation of ZnO_2@Lip-ICG NPs*

ZnO_2@Lip-ICG NPs were synthesised by the thin film-rehydration method. The detailed synthesis steps are presented in Scheme 1. First, the ZnO_2 NPs were prepared using the one-pot precipitation process [49]. Briefly, 5 mmol $Zn(NO_3)_2{\cdot}6H_2O$ and 10 mmol NaOH were separately dissolved in 10 ml methanol. Then, under vigorous agitation, 1.5 ml H_2O_2 and 10 ml NaOH in methanol solution were introduced into 10 ml $Zn(NO_3)_2{\cdot}6H_2O$ in methanol solution. After continuously stirring for 4 h, a white precipitate was gained through centrifugation, and this was washed several times. The product was dried in an oven at 60 °C for 12 h and reserved for further use. The morphology of ZnO_2 NPs was observed by transmission electron microscopy (TEM; JEM-1230, JEOL, Japan). The crystal structure was verified by X-ray diffraction (XRD; X' Pert PRO). Second, 20 mg soy-Lecithin, 5 mg cholesterol, 5 mg DSPE-PEG 2000, 0.5 mg ICG and 5 mg ZnO_2 NPs were dissolved in 10 ml methanol and then evaporated at 37 °C with the help of a rotary evaporator to generate a thin film. After 30 min, phosphate buffered saline (PBS) (pH 7.4) was introduced. Then, sonication was performed for 15 min in an ice bath in the dark to hydrate the lipid film, and the lipid-coated structure was formed. The solution was centrifuged at low speed to remove large particles and the supernatant was collected as ZnO_2@Lip-ICG NPs. The conditions and procedures for ICG loaded liposome (ICG@Lip) and lipid coated ZnO_2 NPs (ZnO_2@Lip) were the same as those for ZnO_2@Lip-ICG.

2.3. *Characterisation of ZnO_2@Lip-ICG NPs*

The particle size and zeta potential of ZnO_2@Lip-ICG NPs were detected through dynamic light scattering (DLS; Zeta Plus, Brookhaven Instruments, USA). Morphology was visualised by TEM. The absorption spectrum and ICG concentration were documented with a UV-vis spectrophotometer (Agilent Cary 60 UV-vis, Santa Clara, CA). The elemental analysis was verified by scanning transmission electron microscopy (STEM; Talos F200X, Netherlands). Fourier transform infrared spectroscopy (FTIR; Bruker VERTEX 70 FTIR spectrophotometer) was employed to characterise the NPs. An 808 nm NIR laser light source induced by a Fibre Coupled Laser System (Laserver, China) was employed to induce the phototherapeutic effect. The loading content of ICG in the liposomes was determined through measuring the unbound concentration of ICG in the supernatant by UV-vis spectroscopy. The loading efficiency was calculated by the following equation: Loading efficiency (%) = (total ICG-unbound ICG)/total ICG. The stability of ZnO_2@Lip-ICG NPs in PBS, FBS and DMEM was monitored by measuring size changes. The stability of ZnO_2@Lip-ICG (with/without laser irradiated) at different pH values was monitored by the release profiles of Zn^{2+} in phosphate buffer under varying pH levels (5.4, 6.5 and 7.4). The Zn^{2+} concentration and release behaviour was evaluated by inductively coupled plasma - optical emission spectrometry (ICP-OES, thermo-fisher iCAP 6300).

2.4. *In vitro photothermal properties and stability*

The photothermal conversion (PTC) performances of each formulation (saline, free ICG, ZnO_2@Lip, ICG@Lip and ZnO_2@Lip-ICG) was detected under 808 nm laser (1.0 W/cm^2) irradiation for 5 min using a fluke thermal imager (Ti29, Fluke, USA). Further, ZnO_2@Lip-ICG NPs containing varing ICG concentrations (initial ICG concentration: 0.625 μg/ml) were treated with an 808 nm laser (1.0 W/cm^2, 5 min). Then, to future investigate the photothermal effect of ZnO_2@Lip-ICG NPs, ZnO_2@Lip-ICG solution (ICG concentration: 2.5 μg/ml) was irradiated under an 808 nm laser with varying power intensities (0.5, 1.0, 1.5 and 2.0 W/cm^2) for 5 min. For the photothermal stability test, the ZnO_2@Lip-ICG aqueous solution was irradiated with an 808 nm laser and then cooled naturally. And the procedure was repeated four times. The PTC efficiency (η) of ZnO_2@Lip-ICG was calculated based on the previously reported method [50,51].

2.5. *In vitro photodynamic property*

DPBF was used to assess the *in vitro* singlet oxygen production ability of ZnO_2@Lip-ICG NPs under continuous 808 nm laser (1.0 W/cm^2) irradiation for 5 min. DPBF can be oxidised by ROS, which changes its structure, decreasing in its absorption at 410 nm. Free ICG, ICG@Lip and ZnO_2@Lip-ICG solutions were mixed rapidly with DPBF (6×10^{-5} M) and stored in the dark. Next, the solutions were irradiated with an 808 nm laser. Subsequently, the absorbance of each solution at 410 nm was recorded at each time point. In addition, the SOSG fluorescence probe was used to verify the ROS generations of

free ICG, ICG@Lip and ZnO_2@Lip-ICG. In brief, 100 μg of SOSG was dissolved in 330 μl of methanol (0.5 mM). Then 10 μl SOSG was added to 1990 μl different solutions.The generated $^1O_2$ was determined by measuring recovered SOSG fluorescence of SOSG (excitation = 494 nm).

2.6. Cell culture

The human NPC cell line CNE-2 was kindly provided by Professor Hongling Jin (HUST, Wuhan, China). Cells were cultured in DMEM high-glucose medium (Hyclone) containing 10% FBS, 100 U/ml penicillin G sodium and 100 μg/ml streptomycin sulphate. Cells were maintained at 37 °C in humidity and 5% CO_2 incubator.

2.7. Intracellular uptake and distribution

To explore the cellular uptake of ZnO_2@Lip-ICG NPs, the CNE-2 cells were seeded into six-well plates at a density of 5.0×10^5 cells per well. The cells were incubated with medium containing ZnO_2@Lip-ICG for 0.5 h, 1 h, 2 h or 4 h after overnight attachment. Next, the cells were washed with chilled PBS and stained with DAPI. The cellular uptake efficiency was investigated by fluorescence microscopy and flow cytometry. For the subcellular distribution of ZnO_2@Lip-ICG NPs, the cells were incubated with medium containing ZnO_2@Lip-ICG for 1 h, 2 h or 4 h after overnight attachment. Then, the cells were exposed to 200 nM LysoTracker Green for 30 min, rinsed with PBS, fixed with 4% paraformaldehyde solution and stained with DAPI. The visualisation was performed using confocal laser scanning microscopy (CLSM).

2.8. Intracellular ROS generation

To discover the generation of ROS, DCFH-DA fluorescent probe was utilised to detect the endogenous ROS levels of ICG@Lip NPs ZnO_2@Lip NPs and ZnO_2@Lip-ICG NPs. 5.0×10^5 CNE-2 cells per well were seeded into a 12-well plate and incubated for 24 h. Next, fresh DMEM medium with varying pH levels (7.4 and 6.5) containing ICG@Lip ZnO_2@Lip or ZnO_2@Lip-ICG was added in place of the old medium. 12 h later, the cells were exposed to DCFH-DA probe (10 μM, 2 ml) for 30 min and then rinsed with PBS. For the groups that received irradiation, the cells were then irradiated with an 808 nm laser at 1.0 W/cm^2 for 5 min. Intracellular ROS images were detected using CLSM. Moreover, flow cytometry was used to collect the quantitative data about the intracellular ROS level.

2.9. In vitro cytotoxic investigation

To explore the *in vitro* cytotoxicity, CNE-2 cells were carefully seeded in a 96-well plate at a density of 5000 cells per well and allowed to grow for 24 h. Next, fresh DMEM medium with varying pH levels (7.4 and 6.5) containing various concentrations of free ICG, ZnO_2@Lip, ICG@Lip or ZnO_2@Lip-ICG was added in place of the old medium. After 4 h incubation, the CNE-2 cells were irradiated in either the presence or absence of an 808 nm laser at 1.0 W/cm^2 for 5 mins and further incubated for another 20 h. The viabilities of the cells were investigated through a CCK-8 assay. Cell apoptosis was further analysed by Calcein-AM and propidium iodide (PI) staining. CNE-2 cells were seeded into a 12-well plate and cultured for 24 h. Then, ICG@Lip and ZnO_2@Lip-ICG were added. After 4 h incubation, the cells in the groups receiving irradiation and then were incubated for another 12 h. Finally, the cells in each group were stained using Calcein-AM and PI for 30 min and were observed with a fluorescence microscope to identify the live and dead cells.

2.10. Western blot analysis

The CNE-2 cells were submitted to the following different treatments: Control pH 7.4, Control pH 6.5, ICG@Lip pH 7.4, ICG@Lip pH 6.5, ZnO_2@Lip-ICG pH 7.4, ZnO_2@Lip-ICG pH 6.5, Control pH 7.4 with laser (808 nm, 1.0 W/cm^2, 5 min), Control pH 6.5 with laser (808 nm, 1.0 W/cm^2, 5 min), ICG@Lip pH 7.4 with laser (808 nm, 1.0 W/cm^2, 5 min), ICG@Lip pH 6.5 with laser (808 nm, 1.0 W/cm^2, 5 min), ZnO_2@Lip-ICG pH 7.4 with laser (808 nm, 1.0 W/cm^2, 5 min), ZnO_2@Lip-ICG pH 6.5 with laser (808 nm, 1.0 W/cm^2, 5 min). Then, the cells were rinsed with ice-cold PBS and lysed with 300 μl extract buffer for 30 min on ice. Proteins in the cell lysate were separated on 10% SDS-PAGE before transfer to PVDF membranes. The membranes were then exposed to blocking buffer for 1 h at room temperature and stained with anti-Caspase-3, anti-Caspase-9, anti-Caspase-12 and anti-Bax antibodies overnight at 4 °C, before staining with corresponding secondary antibodies for 1 h at room temperature. Visualisation was performed using a UVP BioSpectrum Imaging System.

2.11. Biodistribution and pharmacokinetic study

For the biodistribution analysis, free ICG, ICG@Lip and ZnO_2@Lip-ICG NPs were intravenously (i.v.) administered into the CNE-2 tumour-bearing mice. *In vivo* imaging of the tumours at varying time points after nanoparticle administration was performed with the help of an *in vivo* imaging system (IVIS). The mice were then euthanised 24 h post-injection, and the major organs (heart, liver, spleen, lungs and kidney) and tumours were collected for *ex vivo* fluorescence imaging. SD rats were arbitrarily separated into three groups for the pharmacokinetic study to examine the half-lives of free ICG, ICG@Lip and ZnO_2@Lip-ICG NPs in circulation. All rats were administered (i.v.) with free ICG, ICG@Lip or ZnO_2@Lip-ICG (5 mg ICG/kg), respectively. Following NP administration, at predetermined time points (0.5, 1, 2, 4, 8, 24 or 48 h), 300 μl blood samples were collected and assessed via autofluorescence using the IVIS to determine the serum concentrations of free ICG, ICG@Lip and ZnO_2@Lip-ICG NPs.

2.12. Tumour hypoxia status evaluation

In order to monitor the tumour hypoxia status, the CNE-2 tumour-bearing mice were arbitrarily separated into five groups; the groups received three intravenous injections of saline, ZnO_2@Lip, free ICG, ICG@Lip or ZnO_2@Lip-ICG (containing 30 mg liposome/kg), respectively. The mice were

euthanised and the tumours were extracted 24 h after the injection. Immunohistochemical staining of HIF-1α was used to evaluate the hypoxic status of the tumours. The tumour slides were incubated with anti-HIF-1α antibody (dilution 1:100).

2.13. *In vivo photothermal therapeutic efficacy*

Tumour model mice were administered predetermined formulations (saline, ZnO_2@Lip, free ICG, ICG@Lip or ZnO_2@Lip-ICG containing 0.5 mg ICG/kg or 30 mg Lip/kg) every other day for 3 times. After injection for 8 h, the tumour sites of all mice were irradiated with an 808 nm laser (1.0 W/cm^2, 5 min). A fluke thermal imager (Ti29, Fluke, USA) was used to image the tumour sites and evaluate their temperatures.

2.14. *In vivo therapeutic efficacy and safety evaluation*

As shown in Fig. 9A, CNE-2 cells with a density of 1×10^6 were subcutaneously administered to the nude mice. Following tumour growth to a volume of 100 mm^3, the mice were arbitrarily separated into ten groups (five mice per group): (1) saline; (2) ZnO_2@Lip; (3) free ICG; (4) ICG@Lip; (5) ZnO_2@Lip-ICG; (6) saline with 808 laser; (7) ZnO_2@Lip with 808 laser; (8) free ICG with 808 laser; (9) ICG@Lip with 808 laser; and (10) ZnO_2@Lip-ICG with 808 laser. The tumour volumes of each group were assessed every two days after injection with the corresponding pre-determined formulation, using the following calculation formula: $V = A \times B^2/2$ (A: maximum tumour diameter; B: minimum tumour diameter). At the end of the prescribed time, the mice were euthanised and the tumours, along with the major organs, were excised for haematoxylin and eosin (H&E) staining. Approximately 0.2 ml serum was collected from each mouse for biochemistry examination. Liver and kidney functions were assessed via serum ALT and AST levels and BUN and Cr levels, respectively. Apoptotic tumour cells were evaluated with TUNEL staining. HSP 90 expression of tumours was monitored by immunohistochemical staining.

2.15. *Statistical analysis*

All outcomes are expressed as the mean ± standard deviation (SD). Two-group differences were assessed with Student's *t*-test and multi-group differences were assessed with two-way ANOVA. $P<0.05$ was set as significance threshold.

3. Results and discussion

3.1. *Characterisation of ZnO_2@Lip-ICG NPs*

ZnO_2 NPs were prepared by the one-pot precipitation process (Fig. S1A). The resultant ZnO_2 NPs showed a white colour (Fig. S1B) and displayed a high stability after UV irradiation (Fig. S1C). The ZnO_2 NPs consisted of multiple spheres with an average diameter of ~150 nm; this was confirmed by the TEM images (Fig. S1D). In comparison to the standard PDF card (red), the XRD patterns (black) indicated that the ZnO_2 NPs was successfully prepared (Fig. S1E). ZnO_2@Lip-ICG NPs were then synthesised by the thin film-rehydration method. The colour of the ZnO_2@Lip solution changed from white to green after ICG loading (Fig. S2). In Fig. 1A, DLS results revealed that the size of ZnO_2@Lip-ICG was 205.2 nm and the zeta potential of ZnO_2@Lip-ICG was -22.22 mV. TEM showed that ZnO_2@Lip-ICG displayed a typical lipid-coated spherical structure with a ZnO_2 core of about 150 nm and a lipid layer of 15 nm. Compared with the DLS results, the particle size was reduced, potentially due to water evaporation during TEM sample preparation, resulting in a certain degree of collapse [52]. The UV-vis absorption spectrum, STEM and FTIR further validated the structure of ZnO_2@Lip-ICG. The UV-vis spectra results were utilised to confirm the loading of ICG into the NPs. As shown in Fig. 1B, the free ICG showed a characteristic absorption peak at 780 nm; however, no apparent absorption was seen in this region for the Lip and ZnO_2. Compared to the free ICG, ICG@Lip and ZnO_2@Lip-ICG nanoliposomes exhibited enhanced absorption peaks of ICG at 800 nm in the UV-vis-NIR absorption spectrum, with a little red-shift, suggesting the successful loading of ICG in ICG@Lip and ZnO_2@Lip-ICG. The red-shift in ICG absorption (typical ICG absorption peak switching from 780 to 800 nm) confirmed the insert of ICG into the lipid layer [53], which matched better with the 808 nm laser and contributed to the enhanced photothermal performance of ZnO_2@Lip-ICG. The ICG loading efficiency of ZnO_2@Lip-ICG was about 51.5%. To further validate the elemental composition of ZnO_2@Lip-ICG, STEM and elemental mapping images were obtained (Fig. 1C). It was noticed that the Zn and O elements were highly concentrated at the core, while S and P signals were observed at the outer layer, confirming the successful integration of three components (ZnO_2, ICG and Liposomes). In the FTIR spectra, the characteristic absorption peak at 667 cm^{-1} for the indole ring of ICG (Fig. 1D), the vibration peak at 1385 cm^{-1} for the peroxy bond of ZnO_2, and the peaks located at 2852 cm^{-1} and 2933 cm^{-1} assigned to the methyl and methylene groups on the phospholipids were all observed in ZnO_2@Lip-ICG, which demonstrates its hybrid structure.

The stability test showed that the particle size of ZnO_2@Lip-ICG remained unchanged over seven days in PBS, FBS and DMEM, indicating good stability of ZnO_2@Lip-ICG over time (Fig. 1D). Compared to free ICG, whose UV characteristic absorption peak dropped nearly 70% after 48 h, ICG in the ICG@Lip and ZnO_2@Lip-ICG groups was maintained at about 80% after 48 h, indicating that the lipid layer effectively reduced the degradation of ICG (Figs. 1E and S3A–S3D). Consistent with previous studies, these results confirm that ICG can interact with phospholipids in the liposome membrane to improve the stability of ICG.

The stability of ZnO_2@Lip-ICG (with/without NIR irradiated) under different pH was further evaluated through analysis of the release profiles of Zn^{2+} from ZnO_2@Lip-ICG. The malignant proliferation of cancerous cells results in the massive accumulation of metabolic products, which, in turn, reduces the TME pH. NIR (808 nm) irradiation provides sufficient energy to the ICG in the lipid layer such that it produces heat via photochemical transformation,

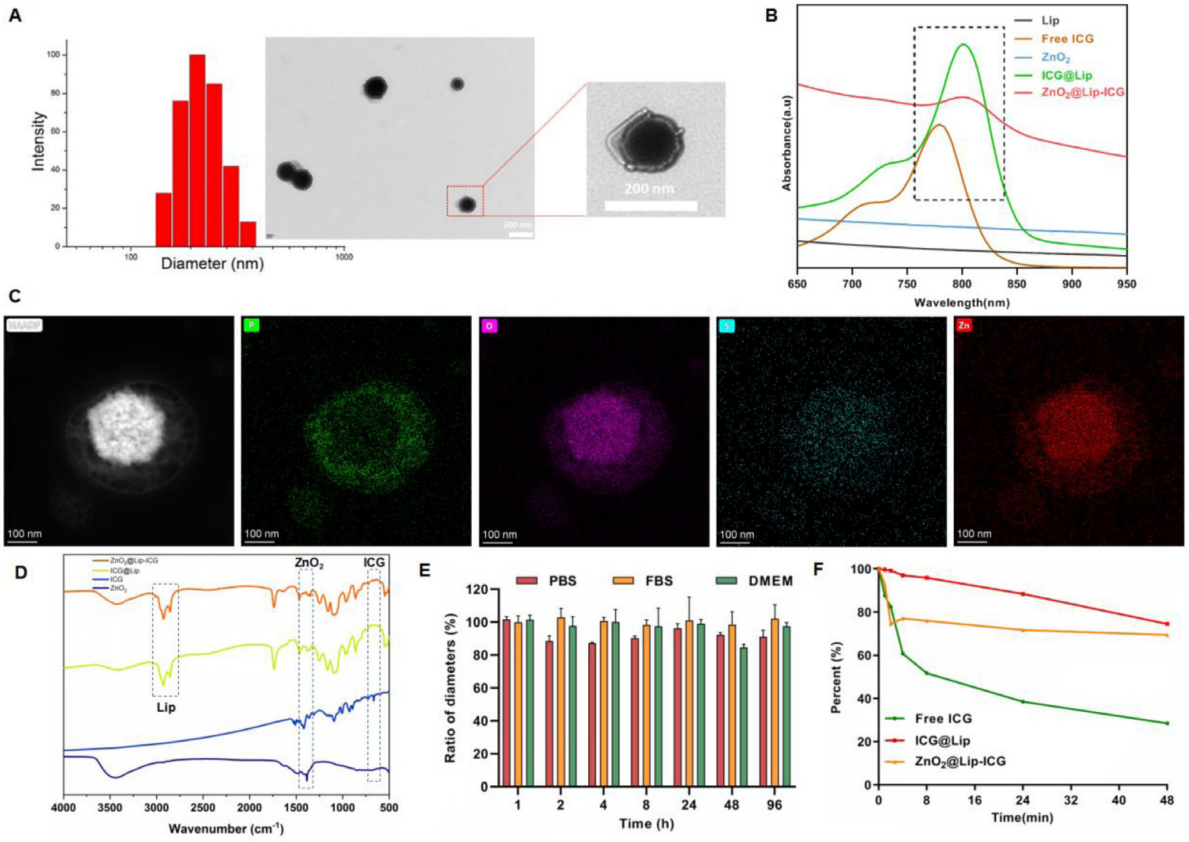

Fig. 1 – Characterisation of ZnO_2@Lip-ICG NPs. **(A) DLS results and TEM image of ZnO_2@Lip-ICG; (B) UV–vis absorption spectra of Lip, free ICG, ZnO_2, ICG@Lip and ZnO_2@Lip-ICG NPs; (C) STEM images and corresponding element mapping of ZnO_2@Lip-ICG nanovehicles (Green: Phosphorus; Purple: Oxygen; Blue: Sulfur; Red: Zinc; Scale bar: 100 nm). (D) FTIR spectra of ZnO_2, ICG, ICG@Lip, and ZnO_2@Lip-ICG NPs; (E) Stability of ZnO_2@Lip-ICG NPs in PBS, FBS and DMEM; (F) Time-dependent degradation of ICG.**

thereby elevating the localised temperature and allowing the liposomes to release Zn^{2+}. Hence, three pH conditions (5.4, 6.5 and 7.4) were chosen to assess the Zn^{2+} release characteristics with/without irradiation. As shown in Fig. S4A, Zn^{2+} released slowly without NIR laser irradiation and the cumulative Zn^{2+} release rate was approximately 24.77% at pH 7.4, 41.18% at pH 6.5 and 53.26% at pH 5.4 at 48 h, respectively. The ZnO_2@Lip-ICG nanovehicle exhibited continued release with a stepwise increase from 24.77% to 53.26% with a pH adjustment from 7.4 to 5.4, which mimics the endogenous and exogenous physiological states, respectively. These data suggest that the nanovehicle release is pH-dependent. Further, the release of Zn^{2+} was significantly accelerated and enhanced with NIR laser irradiation under all pH conditions, confirming that NIR laser irradiation closely regulates drug release [54]. This is likely because the local hyperthermia generated by ICG under irradiation destroyed the lipid membrane and the release of ZnO_2. In an H^+-rich environment, ZnO_2 is highly active and rapidly releases Zn^{2+} (Fig. S4B). Hence, these data demonstrate that both pH and NIR can effectively regulate ZnO_2 release from ZnO_2@Lip-ICG NPs, thereby optimising the anti-neoplastic properties both *in vitro* and *in vivo*.

3.2. *Photothermal and photodynamic performance of ZnO_2@Lip-ICG*

Given the capacity to penetrate into deep tissue, 808 nm NIR laser was employed to induce the PTT/PDT effect of ICG. Following the 808 nm NIR laser irradiation, the temperatures of the saline, ZnO_2@Lip solution and free ICG solution increased slightly by 5.0 °C, 5.4 °C and 12.4 °C, respectively, whereas the temperatures of the ICG@Lip solution and ZnO_2@Lip-ICG solution went up by 22.3 °C and 26.9 °C, respectively; this is attributed to the strong NIR PTC (Fig. 2A&2B). We further investigated the relationship between the temperature and the concentration of the ZnO_2@Lip-ICG solution. The temperature of ZnO_2@Lip-ICG NPs (ICG: 10 μg/ml) increased over 30 °C after irradiation for 5 min, while a slight temperature rise was detected in the saline under similar conditions, implying temperature elevation of ZnO_2@Lip-ICG in an ICG concentration-based manner (Fig. S5A). In addition, the temperature of the ZnO_2@Lip-ICG solution quickly elevated within 5 min in the laser power density increased from 0.5 to 2.0 W/cm^2 (Fig. S5B), indicating that increases in temperature were regulated by power density. After 5 min of irradiation with

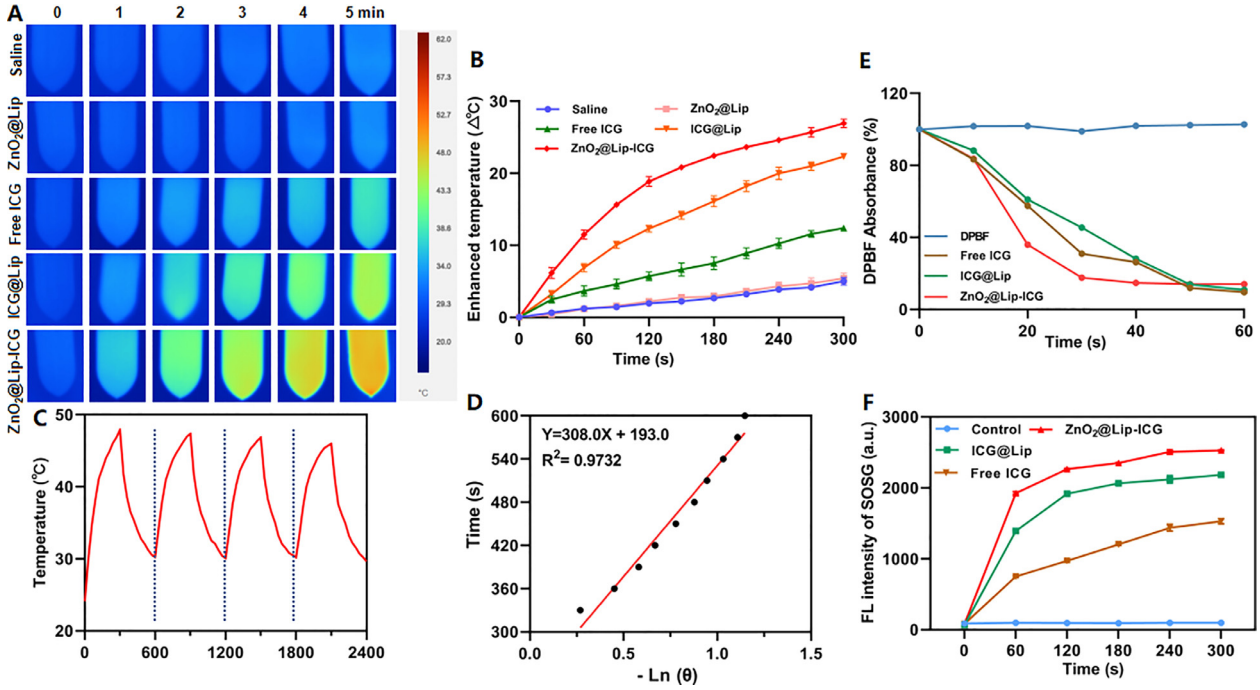

Fig. 2 – Photothermal and photodynamic performance of ZnO_2@Lip-ICG. (A) Thermographic images and (B) temperature elevation profiles of different solutions under 808 nm laser irradiation (1.0 W/cm^2) from 0 to 5 min ($n = 5$); (C) Temperature change of the ZnO_2@Lip-ICG under repeated procedures (4 times) with 808 nm laser-on for 5 min and then laser-off *versus* time. (D) Cooling time *versus* negative natural logarithm of driving force temperature obtained from the cooling stage of (Fig. S5C). (E) Time-dependent ROS generation of free ICG, ICG@Lip and ZnO_2@Lip-ICG irradiated by 808 nm laser for 5 min presented by DPBF degradation. (F) Generation of singlet oxygen by measuring the fluorescence intensity changes of SOSG. The increase of SOSG fluorescence was a result of $^1O_2$ generation.

2.0 W/cm^2, the temperature of the ZnO_2@Lip-ICG solution increased by over 30 °C relative to 0.5 W/cm^2 irradiation, with the latter producing an increase of 14.1 °C. Moreover, photothermal stability of ZnO_2@Lip-ICG was further tested under four cycles of heating and natural cooling, indicating the high photothermal stability(Fig. 2C).The photostability of ZnO_2@Lip-ICG nanoliposomes may attribute to the protective effect of liposomes by isolating the entrapped ICG from surrounding environment and reducing the water-induced transformations [30,55]. For the study of the photothermal performance of the ZnO_2@Lip-ICG NPs, their photothermal conversion efficiency was measured by Roper's method [56]. According to the obtained data, we calculated the photothermal conversion efficiency at 808 nm, and the value was 30.24% (Figs. 2D & S5C). This provides evidence of the excellent effectiveness of ZnO_2@Lip-ICG NPs in converting laser energy to thermal energy.

The singlet oxygen ($^1O_2$) generation of ZnO_2@Lip-ICG NPs *in vitro* was measured using DPBF as a chemical probe. ROS oxidises DPBF and decreases the absorption peak at 410 nm [57]. Accordingly, different solutions (free ICG, ICG@Lip and ZnO_2@Lip-ICG) mixed with DPBF were irradiated with an 808 nm laser (1.0 W/cm^2, 5 min) in the dark. There was no apparent change in DPBF absorbance at 410 nm under laser irradiation, suggesting that the DPBF did not affect the ROS generation ability (Figs. 2E & S6A). Compared with the free ICG and ICG@Lip groups, the ZnO_2@Lip-ICG group exhibited a sharp decrease within 30 s, owing to the O_2 self-supplying PDT effect by the decomposition of ZnO_2 (Figs. 2E & S6B–S6D). For ICG and ICG@Lip, it took 50 s to achieve same DPBF degradation extent. The SOSG fluorescence probe was used to verify the ROS generations of free ICG, ICG@Lip and ZnO_2@Lip-ICG solutions. The singlet oxygen production efficiency of different types of nanoparticles, which could be determined by the recovered SOSG fluorescence. As shown in Fig. 2F, obvious enhancement of fluorescence intensity generated from ZnO_2@Lip-ICG nanoliposomes compared to the free ICG and ICG@Lip groups, indicating the contribution of ZnO_2 to the enhanced photodynamic effect. These results further demonstrate that ZnO_2@Lip-ICG nanoplatforms can enhance ROS production and produce an outstanding PDT effect. According to these results, it can be inferred that the ZnO_2@Lip-ICG nanoplatforms can be employed as efficient NIR-mediated PTT/PDT agents for precise tumour phototherapy.

3.3. *Intracellular uptake and distribution*

To further verify the cellular uptake properties, CNE-2 cells were incubated with ZnO_2@Lip-ICG NPs with the equivalent concentration of ICG 10 μg/ml for varying durations (0.5, 1, 2 and 4 h, respectively). As can be seen by the

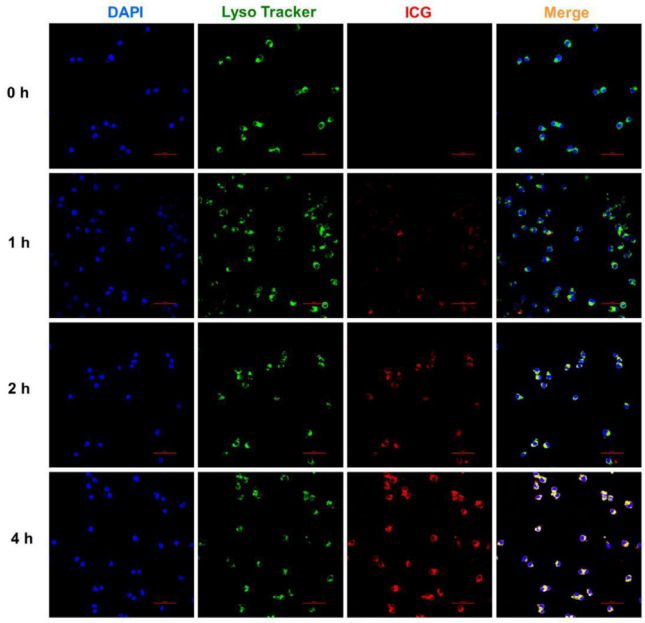

Fig. 3 – Subcellular localisation of ZnO_2@Lip-ICG NPs. Confocal fluorescence images of CNE-2 cells after incubated with ZnO_2@Lip-ICG, Lyso Tracker and DAPI. Blue: DAPI; Green: Lyso Tracker; Red: ICG; Scale bar: 50 μm.

fluorescence microscopy and flow cytometry results, a time-dependent fluorescence increase in CNE-2 cells was observed (Fig. S7A–S7C). It is widely believed that the lysosomal pathway is strongly associated with nanosystem endocytosis. Therefore, we further examined the internalisation behaviour of ZnO_2@Lip-ICG NPs via the endocytic pathway. As shown in Fig. 3, yellow fluorescence due to the co-localisation of acidic organelles (green) and ICG (red) was observed after the incubation of ZnO_2@Lip-ICG for two hours, verifying involvement of the endocytic pathway. At 4 h, more red fluorescence was observed in the cell and was co-localised with green fluorescence (lysosome); further, parts of the red fluorescence separated from the yellow fluorescence and entered the cytoplasm, reflecting ICG escape from lysosomes. As such, ZnO_2 degrades quickly and more H_2O_2 is generated under the acid environment of the lysosomes, benefitting the following PTT treatment triggered by NIR.

3.4. *Intercellular ROS generation*

To further confirm singlet oxygen generation, a ROS probe (DCFH-DA, green) was employed to measure endogenous ROS levels in CNE-2 cells under different treatments. For ICG@Lip, due to the limited oxygen and slow generation of ROS, weak green fluorescence was observed after NIR irradiation at both pH 7.4 and 6.5. For ZnO_2@Lip group, the ROS level only slightly increased after NIR irradiation under pH 6.5 condition, attributing to the decomposition of ZnO_2 under acidic condition. For ZnO_2@Lip-ICG group without NIR irradiation, weak green fluorescence was noted due to its H_2O_2 generation capability. After NIR irradiation, the ZnO_2@Lip-ICG group with NIR irradiation displayed intense green fluorescence, especially at pH 6.5, indicating tremendous ROS generation enhanced by O_2 self-supply from ZnO_2 (Fig. 4).

Additionally, we analysed the quantitative data for the intracellular ROS level through flow cytometry, as shown in Fig. S8. The results proved that the ROS levels of ZnO_2@Lip-ICG with 808 nm laser irradiation under pH 6.5 condition was much higher than other groups, which is consistent with the image data. These results suggest that the ZnO_2@Lip-ICG nanosystem efficiently generates ROS in CNE-2 cells and exhibits a low-pH-dependent release tendency, which is suitable for tumour treatment owing to the weak acidic tumour microenvironment.

3.5. *In vitro cytotoxicity and apoptosis*

Cytotoxicity assays of multiple nanoparticles were performed on CNE-2 cells using the CCK-8 method. Cytotoxicity assays of free ICG, ZnO_2@Lip, ICG@Lip, ZnO_2@Lip-ICG, free ICG with irradiation, ZnO_2@Lip with irradiation, ICG@Lip with irradiation, and ZnO_2@Lip-ICG with irradiation at pH 7.4 or 6.5 were performed Fig. 5A illustrated that free ICG and ICG@Lip produced negligible cytotoxicity to CNE-2 cells at pH 7.4 and pH 6.5 without NIR irradiation. After irradiation, the cell viabilities of free ICG and ICG@Lip were slightly decreased at pH 7.4 and 6.5.

For ZnO_2@Lip group, it was exhibited a limited cell inhibition after irradiation even at pH 6.5 with irradiation. The survival rate of CNE-2 cells exposed to ZnO_2@Lip-ICG with laser irradiation showed a gradual reduction with increasing ICG concentration, indicating a dose-dependent therapeutic effect. Moreover, the cell destroying capacity of ZnO_2@Lip-ICG increased with a decrease in pH from 7.4 to 6.5, and the IC_{50} values at pH 7.4 and 6.5 were 2.03 and 0.34 μg/ml, respectively. This is consistent with the ROS generation results, demonstrating a pH-dependent PDT therapeutic effect of ZnO_2@Lip-ICG. It is also worth noting that the IC_{50} values of ZnO_2@Lip-ICG without laser irradiation at pH 7.4 and 6.5 were 10.77 and 5.23 μg/ml, respectively, exhibiting an obvious pH-dependent nature due to the ZnO_2. At pH 7.4, ZnO_2 decomposed slowly, and only at high concentrations did it produce obvious cytotoxicity against cells ($IC50_{ZnO2}$ 111.79 μg/ml for ZnO_2@Lip-ICG). At pH 6.5, ZnO_2 degraded rapidly to form H_2O_2 and Zn^{2+}. Zn^{2+} inhibits the electronic respiratory chain and induces the production of ROS. H_2O_2 is a type of ROS that can also cause damage to cells accompanied by the capability of oxygen generation. And thus, a low IC_{50} value was observed ($IC50_{ZnO2}$ 55.86 μg/ml), which was higher than reported PVP-modified ZnO_2 NPs possibly due to the larger size and lipid coated surface of ZnO_2@Lip-ICG [58]. These findings further demonstrated that the ZnO_2@Lip-ICG nanoplatform was the most efficacious in destroying CNE-2 cells, as compared to the other groups, due to the self-oxygenated nature and synergistic effect. The apoptosis of CNE-2 cells induced by ZnO_2@Lip-ICG was further assessed by fluorescence costaining of live and dead cells with Calcein-AM and PI, respectively. The living cells were stained green and dead cells red (Figs. 5B & S9). Consistent with CCK-8 results, cells exposed to ZnO_2@Lip-ICG NPs at pH 6.5 and 808 nm laser exhibited massive cell death, evidenced by strong red fluorescence. By contrast, the

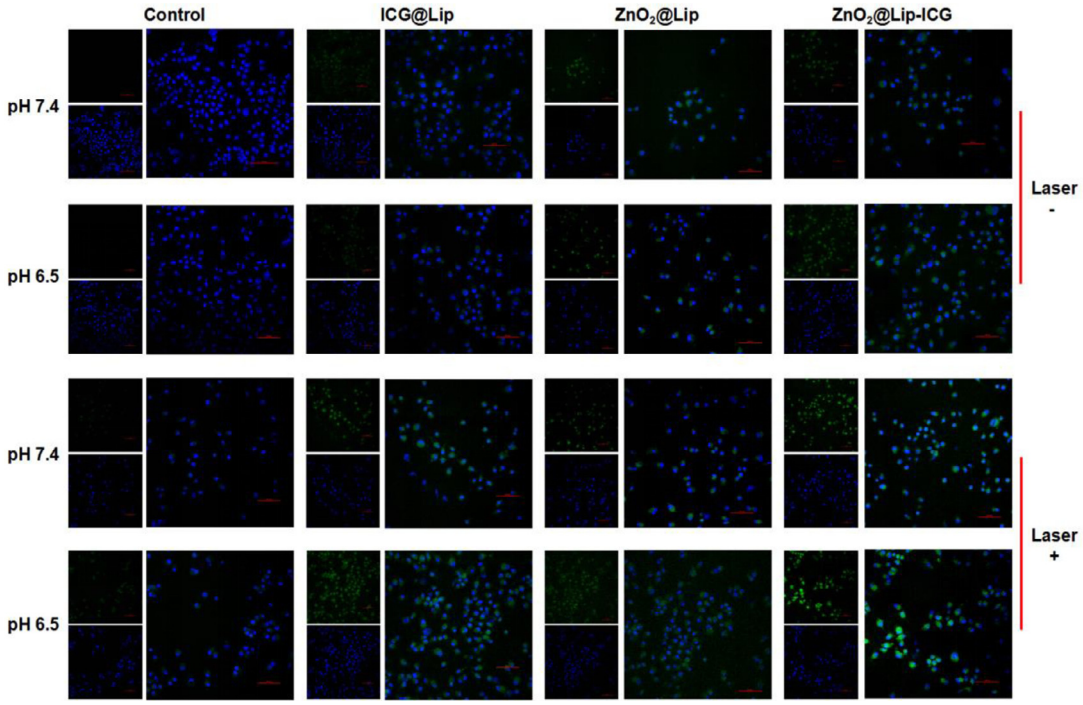

Fig. 4 – Intercellular ROS Generation. **The intracellular ROS generation of ICG@Lip, ZnO_2@Lip and ZnO_2@Lip-ICG NPs detected by DCFH-DA probe after various treatments. Blue: DAPI; Green: DCFH-DA. Scale bar: 100 μm.**

Table 1 – Summarised pharmacokinectic parameters of free ICG, ICG@Lip and ZnO_2@Lip-ICG NPs.

Parameters	Unit	Free ICG	ICG@Lip	ZnO_2@Lip-ICG
AUC_{0-t}	mg•l/h	1.22 ± 0.071	10.64 ± 0.17	9.76 ± 0.15
MRT_{0-t}	h	7.33 ± 0.77	11.63 ± 0.23	11.96 ± 0.42
$T_{1/2}$	h	12.89 ± 0.51	11.40 ± 1.13	9.95 ± 0.46
CL	l/h/kg	3.88 ± 0.21	0.45 ± 0.013	0.50 ± 0.009

control group showed no detectable damage, confirming that the ZnO_2@Lip-ICG exhibited excellent antitumour efficiency. We further investigated the mechanism of apoptosis induced by ZnO_2@Lip-ICG. The increased levels of apoptosis-related proteins (Bax, Caspase-3, Caspase-9 and Caspase-12) evidently showed that the coexistence of ZnO_2@Lip-ICG, NIR and acidity was essential for generating ROS and regulating cancer cell death (Fig. 5C).

3.6. *Pharmacokinetics and biodistribution*

To select the optimal duration for cancer therapy, *in vivo* NIR fluorescence imaging was conducted to identify nanomaterial accumulation in tumour tissues of CNE-2 tumour-bearing mice. Fluorescence imaging offers a unique approach for visualising the pharmacokinetics (PK) and biodistribution of ZnO_2@Lip-ICG throughout the body. As shown in Fig. 6A&6B, free ICG was quickly cleared in plasma, while the lipid bilayer of ICG@Lip and ZnO_2@Lip-ICG enhanced the stability, and resulted similar PK parameters of for the two systems. Although the half-lives of ICG@Lip and ZnO_2@Lip-ICG NPs were a little short compared with free ICG, the area under the curve (AUC_{0-t}) and mean retention time (MRT_{0-t}) were greatly increased, by about 8.0 and 1.6 times, respectively. The clearance (CL) of ICG@Lip and ZnO_2@Lip-ICG NPs was decreased 8.7 and 7.7 times, respectively (Table 1). The enhanced PK property of ZnO_2@Lip-ICG lays a solid foundation for satisfactory *in vivo* therapeutic effects.

After intravenously injection of free ICG, ICG@Lip or ZnO_2@Lip-ICG, the fluorescence signals of the ZnO_2@Lip-ICG NPs group in the tumour areas were increased gradually, reaching a maximum at 8 h post-injection and then slowly decreasing. In contrast, in the free ICG group, the fluorescence signals in the tumour regions were temporarily increased and then decreased rapidly, without showing specific aggregation. The above results indicated that free ICG was characterised by quick clearance and tumour-targeting deficiency, while ICG@Lip and ZnO_2@Lip-ICG NPs exhibited prominent tumour retention effects (Fig. 6C). The accumulation of ZnO_2@Lip-ICG NPs might be related to their EPR effect and good stability, as the liposome nanocarrier can prevent ICG binding to plasma proteins, thereby improving the circulation time of the NPs. Moreover, it has been reported that long-circulating NPs ranging in size from 100 to 200 nm can extravasate

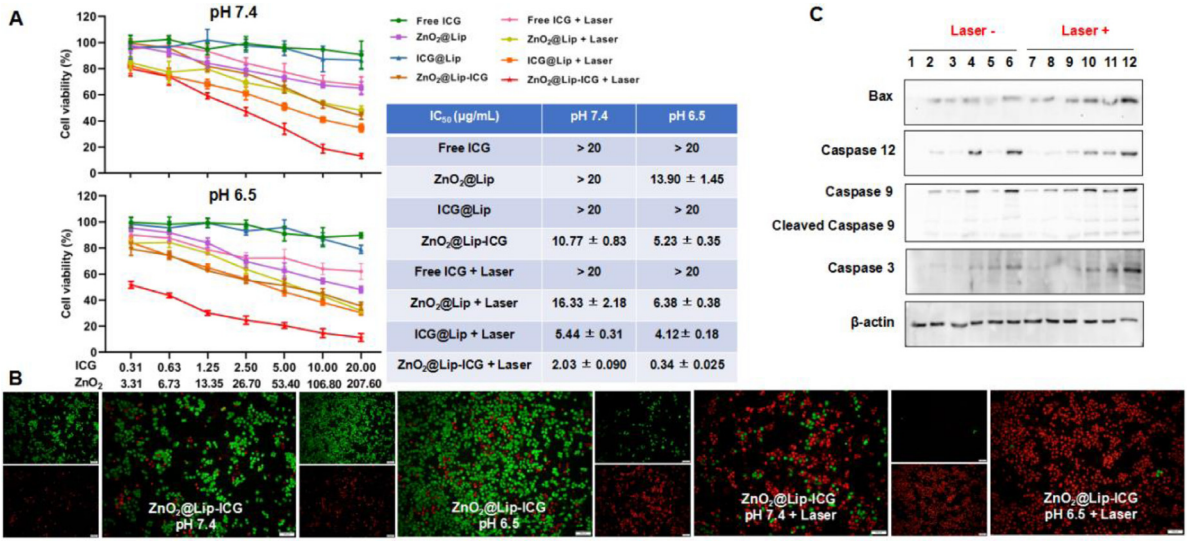

IC_{50} (μg/mL)	pH 7.4	pH 6.5
Free ICG	> 20	> 20
ZnO_2@Lip	> 20	13.90 ± 1.45
ICG@Lip	> 20	> 20
ZnO_2@Lip-ICG	10.77 ± 0.83	5.23 ± 0.35
Free ICG + Laser	> 20	> 20
ZnO_2@Lip + Laser	16.33 ± 2.18	6.38 ± 0.38
ICG@Lip + Laser	5.44 ± 0.31	4.12± 0.18
ZnO_2@Lip-ICG + Laser	2.03 ± 0.090	0.34 ± 0.025

Fig. 5 – Cytotoxicity and apoptosis investigation. **(A) *In vitro* cytotoxicity assays of free ICG, ZnO_2@Lip, ICG@Lip and ZnO_2@Lip-ICG with or without 808 nm laser irradiation (1.0 W/cm^2) at pH 7.4 or 6.5 ($n = 3$); (B) The apoptosis of CNE-2 cells after various treatments was detected by calcein AM/PI staining (Green: live cells, Red: dead cells. Scale bar: 100 μm.); (C) The expression levels of Bax, Caspase-3, Caspase-9 and Caspase-12 in CNE-2 cells after different treatments (1: Control pH7.4; 2: Control pH6.5; 3: ICG@Lip pH7.4; 4: ICG@Lip pH6.5; 5: ZnO_2@Lip-ICG pH 7.4; 6: ZnO_2@Lip-ICG pH 6.5; 7: Control+Laser pH 7.4; 8: Control+Laser pH 6.5; 9: ICG@Lip+Laser pH 7.4; 10: ICG@Lip+Laser pH 6.5; 11: ZnO_2@Lip-ICG+Laser pH 7.4; 12: ZnO_2@Lip-ICG+Laser pH 6.5).**

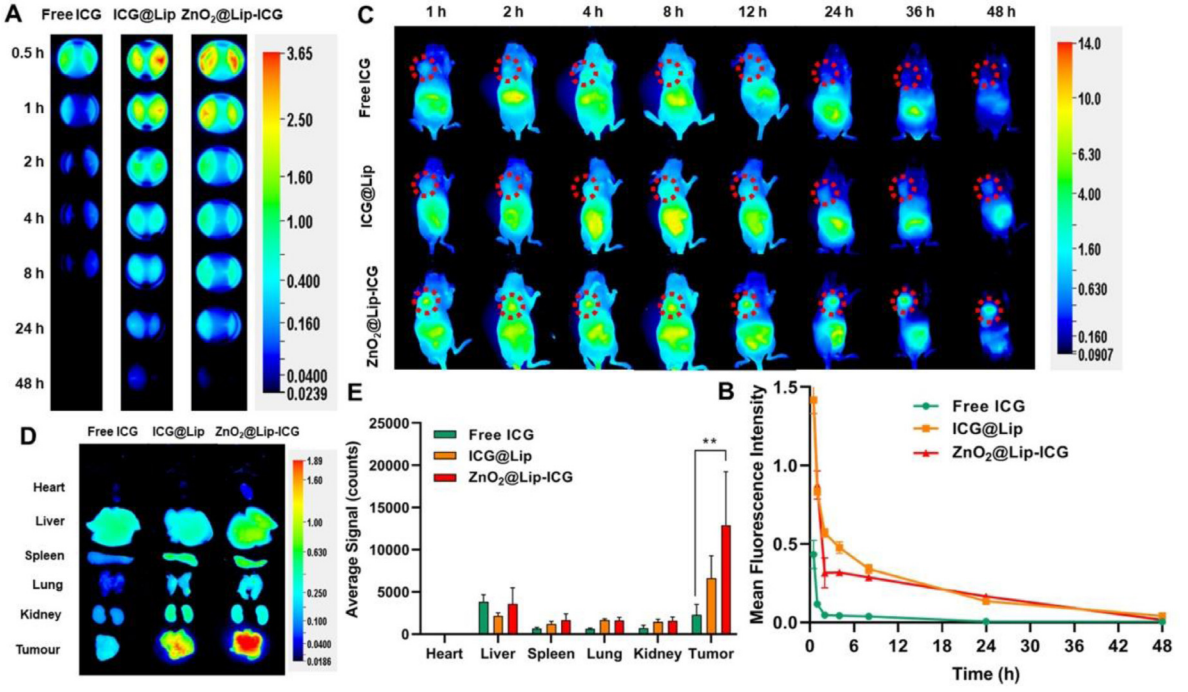

Fig. 6 – *In vivo* pharmacokinetic and biodiatribution study. **(A) Fluorescence intensity of rat's blood at the indicated time points after i.v. injection of free ICG, ICG@Lip and ZnO_2@Lip-ICG; (B) Concentration-Time profiles of free ICG, ICG@Lip and ZnO_2@Lip-ICG ($n = 3$); (C) Fluorescence images of CNE-2 tumour-bearing mice after i.v. injection of free ICG, ICG@Lip and ZnO_2@Lip-ICG (5 mg ICG/kg) at the indicated time points; (D) Fluorescence imaging of major organs and tumours from CNE-2 tumour-bearing mice at 24 h post-injection; (E) The average fluorescence signal intensity of the tumours and major organs ($n = 3$), ** $P < 0.01$.**

from vessels [59,60]. Here, the diameter of the ZnO_2@Lip-ICG NPs was below 200 nm, allowing them to successfully diffuse through the interstitial space to reach the tumour site. To validate tumour accumulation, tumour-bearing mice were euthanised 24 h after NP administration and the major organs were harvested for *ex vivo* imaging. The results suggested that ZnO_2@Lip-ICG NPs accumulated at the tumour region, exhibiting much higher accumulation than that observed with free ICG (Fig. 6D & 6E). Further, a small amount of free ICG and ZnO_2@Lip-ICG accumulated in the liver and spleen, owing to the interaction with reticuloendothelial system (RES).

We further tested the *in vivo* photothermal effect of ZnO_2@Lip-ICG NPs. To shed more light on the PTT effect *in vivo*, the tumours were irradiated 8 h post-injection and the temperatures in the tumour regions were recorded. As shown in Fig. 7A and 7B, the groups that received saline, ZnO_2@Lip or free ICG exhibited only moderate temperature rises (about 3 °C). In contrast, in the ICG@Lip and ZnO_2@Lip-ICG groups, remarkable increases in localised temperature were observed, with the peak temperature reaching 52.1 °C and 54.0 °C, respectively; these temperatures are higher than the threshold value (42 °C) of PTT. In addition, we detected the expression of heat shock protein 90 (HSP 90) by immunohistochemical staining. HSP 90 served as a critical protein to induce thermotolerance for tumour cells under hyperthermia [61]. As shown in Fig. S10, the expression of HSP 90 was remarkably up-regulated both in the ICG@Lip + laser and ZnO_2@Lip-ICG + laser groups owing to the local hyperthermia. In contrast, almost no HSP positive tumour cells were detected in the groups without irradiation. All above results showed that ICG@Lip and ZnO_2@Lip-ICG groups displayed similar temperature profiles after irradiation. It is further verified that there is no significant difference of photothermal efficiency between ICG@Lip and ZnO_2@Lip-ICG.

Immunohistochemical hypoxia-inducible factor-1α (HIF-1α) staining was performed to assess the capability of ZnO_2 to relieve tumour hypoxia. Tumour hypoxia-driven upregulation of HIF-1α can serve as an indirect predictor of a hypoxic microenvironment [62,63]. HIF-1α-positive tumour cells manifested as brown spots. As expected, only scattered HIF-1α-positive cells were detected in the ZnO_2@Lip- and ZnO_2@Lip-ICG-treated tumours, whereas the three other groups (saline, free ICG and ICG@Lip) exhibited significant HIF-1α-positive cells in the tumour tissue sections (Fig. S11). These findings indicated that ZnO_2-loaded nanoliposomes effectively alleviated the hypoxic state of tumours, which could supply enough oxygen for ICG to achieve a highly efficient PDT.

3.7. *In vivo therapeutic efficacy and biosafety evaluation*

The antitumour properties and biosafety of ZnO_2@Lip-ICG with irradiation were explored in CNE-2 tumour-bearing mice. As shown in Fig. 8B–8D, in the groups without laser or ICG, the tumour growth was in general not different from control group, while tumour growth was significantly inhibited in the ZnO_2@Lip-ICG + laser group compared with the other groups, especially the ICG@Lip + laser group. We have previously confirmed that ICG@Lip and ZnO_2@Lip-ICG had no obvious differences in photothermal efficiency. Therefore, the difference in therapeutic efficacies of ICG@Lip and ZnO_2@Lip-ICG was related to the enhanced PDT effect rather than the PTT effect. The tumour inhibition rates of the

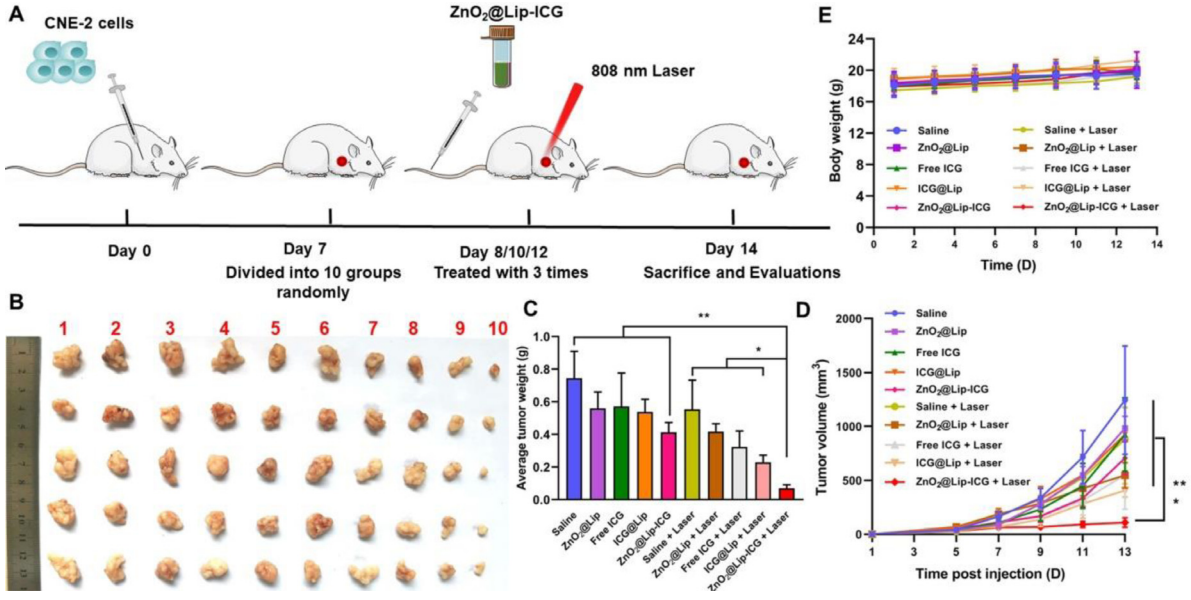

Fig. 8 – *In vivo* antitumour efficacy in tumour-bearing BABL/C nude mice. (A) Schematic illustration of *in vivo* antitumour efficacy of ZnO_2@Lip-ICG NPs; (B) photograph of tumour tissues; (1: Saline; 2: ZnO_2@Lip; 3: Free ICG; 4: ICG@Lip; 5: ZnO_2@Lip-ICG; 6: Saline+Laser; 7: ZnO_2@Lip+Laser; 8: Free ICG+Laser; 9: ICG@Lip+Laser; 10: ZnO_2@Lip-ICG+Laser); (C) Tumour weight, (D) tumour volume and (E) body weight of CNE-2 tumour-bearing mice in each group ($n = 5$), * $P < 0.05$, ** $P < 0.01$.

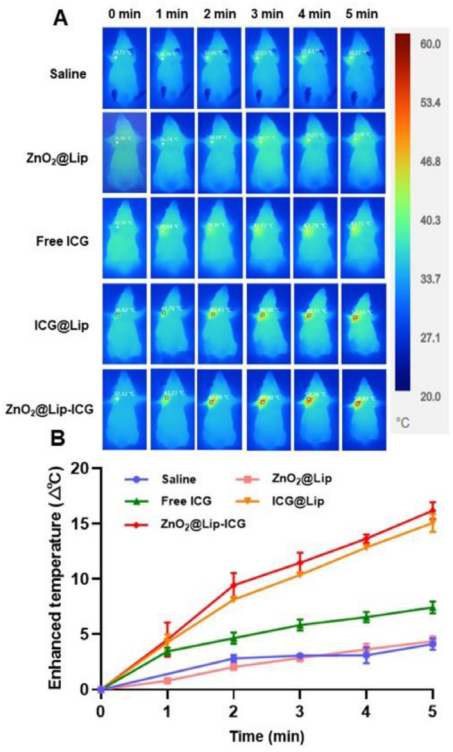

Fig. 7 – *In vivo* photothermal effects of ZnO_2@Lip-ICG. (A) Thermographic images of CNE-2 tumour-bearing mice after 24 h injection of saline, ZnO_2@Lip, free ICG, ICG@Lip and ZnO_2@Lip-ICG under 808 nm laser (1.0 W/cm^2) irradiated during 5 min; (B) The enhanced temperature profiles in the tumour sites during NIR laser irradiation ($n = 3$).

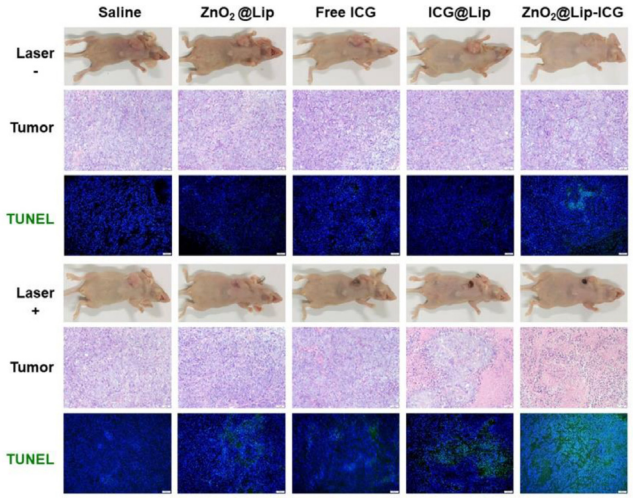

Fig 9 – Representative digital photographs of CNE-2 tumour-bearing mice before euthanisation; H&E (Sacle bar: 50 μm) and TUNEL staining of tumour tissues (Blue: DAPI, Green: TUNEL; Scale bar: 100 μm).

ICG@Lip+laser and ZnO_2@Lip-ICG+laser groups were 67.4% and 84.9%, respectively, demonstrating that the oxygen self-supported strategy effectively enhanced PTT/PDT efficiency and thus, suppressed tumour development. Moreover, no noticeable weight changes were observed in any of the groups receiving the various treatments (Fig. 8E), suggesting negligible systemic toxicity of the nanoliposomes. When taken together with the above-described *in vivo* results, these findings further verify the superior therapeutic efficacy of ZnO_2@Lip-ICG over ICG@Lip, due to the ability of ZnO_2

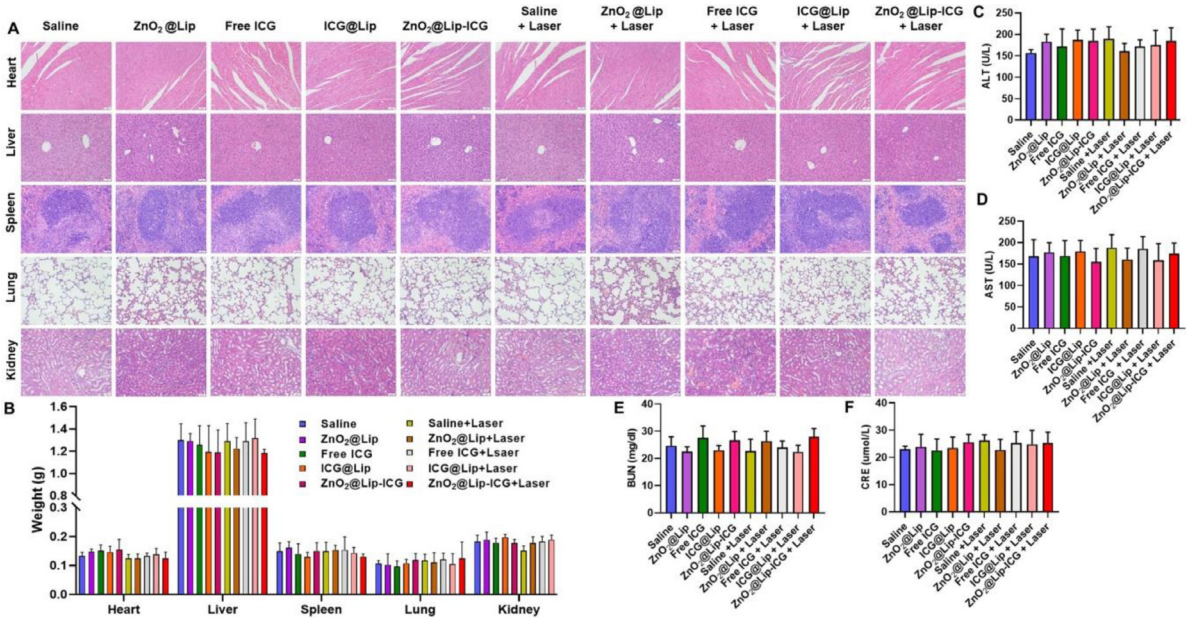

Fig. 10 – Safety evaluation *in vivo*. (A) Representative H&E staining of the major organs of CNE-2 tumour-bearing mice treated with various nanoparticles. Scale bar: 50 μm. (B) The weights of the main organs separated from CNE-2 tumour-bearing mice with different treatments ($n = 5$). (C-F) The blood index of ALT, AST, BUN, and CRE of tumour-bearing mice with different treatments ($n = 5$).

to continuously produce oxygen, thus improving the O_2-dependent PDT effect.

H&E and TUNEL staining were employed to explore the underlying mechanisms of tumour growth suppression. As demonstrated in Fig. 9, extensive tumour necrosis and severe karyopyknosis were detected in tumours treated with ZnO_2@Lip-ICG and laser irradiation. Notably, the ZnO_2@Lip-ICG + laser irradiation group displayed discrete green fluorescence, evidencing severe tissue apoptosis. These results indicated that ZnO_2@Lip-ICG had excellent antitumour effects. In order to verify whether this drug delivery system has a general anti-tumour effect, we also tested the therapeutic efficacy of ZnO_2@Lip-ICG in H22 tumour-bearing mice. The results were consistent with the CNE-2 tumour model (Fig. S12).

To evaluate the biosafety of the ZnO_2@Lip-ICG NPs, we also conducted a thorough examination of the *in vivo* toxicity. H&E staining of major organs (liver, heart, spleen, kidneys and lungs) in all groups showed no appreciable abnormalities (Fig. 10A) and there were no significant differences in major organ weights amongst the groups receiving the various treatments (Fig. 10B). This demonstrated that ZnO_2@Lip-ICG caused minimal toxicity to the major organs. Moreover, the liver function and kidney function indices were within the normal reference ranges, indicating that ZnO_2@Lip-ICG NPs did not induce apparent hepatic or renal toxicity (Fig. 10C–10F). Taken together, the above results demonstrate that ZnO_2@Lip-ICG nanosystems have good biocompatibility and can serve as an excellent candidate for cancer therapy in the future.

4. Conclusion

In summary, we successfully designed and synthesised a new TME-responsive nanotherapeutic agent, ZnO_2@Lip-ICG, which regulates the hypoxic TME and delivers ROS to cancer cells. Systematic *in vitro* and *in vivo* examinations illustrated that ZnO_2@Lip-ICG selectively accumulates within tumour sites and the hypoxic tumour environment is effectively eliminated via persistent O_2 production by ZnO_2. This approach presents a highly efficacious system that facilitates the simultaneous relief of tumour hypoxia along with enhanced PDT. Meanwhile, the *in vivo* safety evaluation further confirms that ZnO_2@Lip-ICG exhibits superior biocompatibility. Thus, this new O_2 self-sufficient nanoplatform can serve as an excellent theranostic system for highly efficacious cancer treatment.

Conflicts of interest

The authors declare that they have no competing interests.

Acknowledgments

The authors thank the Analytical and Testing Centre of HUST for FTIR, XRD and TEM measurements.This work was supported by the National Natural Science Foundation of China (No. 81771002, 82071057 and 82000988).

Supplementary materials

Supplementary material associated with this article can be found, in the online version, at doi:10.1016/j.ajps.2022.01.002.

REFERENCES

[1] Chen YP, Chan ATC, Le QT, Blanchard P, Sun Y, Ma J. Nasopharyngeal carcinoma. Lancet 2019;394:64–80.
[2] Lee HM, Okuda KS, Gonzalez FE, Patel V. Current perspectives on nasopharyngeal carcinoma. Adv Exp Med Biol 2019;1164:11–34.
[3] Guo R, Mao YP, Tang LL, Chen L, Sun Y, Ma J. The evolution of nasopharyngeal carcinoma staging. Br J Radiol 2019;92:20190244.
[4] Liu Z, Wang D, Li J, Jiang Y. Self-assembled peptido-nanomicelles as an engineered formulation for synergy-enhanced combinational SDT, PDT and chemotherapy to nasopharyngeal carcinoma. Chem Commun 2019;55:10226–9 (Camb).
[5] Wang HY, Chang YL, To KF, Hwang JS, Mai HQ, Feng YF, et al. A new prognostic histopathologic classification of nasopharyngeal carcinoma. Chin J Cancer 2016;35:41.
[6] Qiu Y, Guo Z, Han L, Yang Y, Li J, Liu S, et al. Network-level dysconnectivity in patients with nasopharyngeal carcinoma (NPC) early post-radiotherapy: longitudinal resting state fMRI study. Brain Imaging Behav 2018;12:1279–89.
[7] Wu VW, Lam YN. Radiation-induced temporo-mandibular joint disorder in post-radiotherapy nasopharyngeal carcinoma patients: assessment and treatment. J Med Radiat Sci 2016;63:124–32.
[8] Li X, Lovell JF, Yoon J, Chen X. Clinical development and potential of photothermal and photodynamic therapies for cancer. Nat Rev Clin Oncol 2020;17:657–74.
[9] Horne TK, Cronje MJ. Cancer tissue classification, associated therapeutic implications and PDT as an alternative. Anticancer Res 2017;37:2785–807.
[10] Wang K, Lu J, Li J, Gao Y, Mao Y, Zhao Q, et al. Current trends in smart mesoporous silica-based nanovehicles for photoactivated cancer therapy. J Control Release 2021;339:445–72.
[11] Kwiatkowski S, Knap B, Przystupski D, Saczko J, Kedzierska E, Knap-Czop K, et al. Photodynamic therapy - mechanisms, photosensitizers and combinations. Biomed Pharmacother 2018;106:1098–107.
[12] Dolmans DE, Fukumura D, Jain RK. Photodynamic therapy for cancer. Nat Rev Cancer 2003;3:380–7.
[13] Son J, Yi G, Yoo J, Park C, Koo H, Choi HS. Light-responsive nanomedicine for biophotonic imaging and targeted therapy. Adv Drug Deliv Rev 2019;138:133–47.
[14] Palmieri V, De Maio F, De Spirito M, Papi M. Face masks and nanotechnology: keep the blue side up. Nano Today 2021;37:101077.
[15] Thakur NS, Patel G, Kushwah V, Jain S, Banerjee UC. Facile development of biodegradable polymer-based nanotheranostics: hydrophobic photosensitizers delivery, fluorescence imaging and photodynamic therapy. J Photochem Photobiol B 2019;193:39–50.
[16] Simoes JCS, Sarpaki S, Papadimitroulas P, Therrien B, Loudos G. Conjugated photosensitizers for imaging and PDT in cancer research. J Med Chem 2020;63:14119–50.

[17] Scherhag A, Kaden JJ, Kentschke E, Sueselbeck T, Borggrefe M. Comparison of impedance cardiography and thermodilution-derived measurements of stroke volume and cardiac output at rest and during exercise testing. Cardiovasc Drugs Ther 2005;19:141–7.
[18] Bonora BM, Vigili de Kreutzenberg S, Avogaro A, Fadini GP. Effects of the SGLT2 inhibitor dapagliflozin on cardiac function evaluated by impedance cardiography in patients with type 2 diabetes. Secondary analysis of a randomized placebo-controlled trial. Cardiovasc Diabetol 2019;18:106.
[19] Zhang D, Song XJ, Li SY, Wang SY, Chen BJ, Bai XD, et al. Evaluation of liver function and electroacupuncture efficacy of animals with alcoholic liver injury by the novel imaging methods. Sci Rep 2016;6:30119.
[20] Tralhao JG, Hoti E, Oliveiros B, Abrantes AM, Botelho MF, Castro-Sousa F. Intermittent pringle maneuver and hepatic function: perioperative monitoring by noninvasive ICG-clearance. World J Surg 2009;33:2627–34.
[21] Hoffmann C, Compton F, Schafer JH, Steiner U, Fuller TF, Schostak M, et al. Intraoperative assessment of kidney allograft perfusion by laser-assisted indocyanine green fluorescence videography. Transplant Proc 2010;42:1526–30.
[22] Chen QY, Xie JW, Zhong Q, Wang JB, Lin JX, Lu J, et al. Safety and efficacy of indocyanine green tracer-guided lymph node dissection during laparoscopic radical gastrectomy in patients with gastric cancer: a randomized clinical trial. JAMA Surg 2020;155:300–11.
[23] Chen WR, Zhu WG, Dynlacht JR, Liu H, Nordquist RE. Long-term tumor resistance induced by laser photo-immunotherapy. Int J Cancer 1999;81:808–12.
[24] Chen WR, Adams RL, Bartels KE, Nordquist RE. Chromophore-enhanced *in vivo* tumor cell destruction using an 808-nm diode laser. Cancer Lett 1995;94:125–31.
[25] Sawa M, Awazu K, Takahashi T, Sakaguchi H, Horiike H, Ohji M, et al. Application of femtosecond ultrashort pulse laser to photodynamic therapy mediated by indocyanine green. Br J Ophthalmol 2004;88:826–31.
[26] Barth BM, IA E, Shanmugavelandy SS, Kaiser JM, Crespo-Gonzalez D, DiVittore NA, et al. Targeted indocyanine-green-loaded calcium phosphosilicate nanoparticles for *in vivo* photodynamic therapy of leukemia. ACS Nano 2011;5:5325–37.
[27] Ma Y, Tong S, Bao G, Gao C, Dai Z. Indocyanine green loaded SPIO nanoparticles with phospholipid-PEG coating for dual-modal imaging and photothermal therapy. Biomaterials 2013;34:7706–14.
[28] Saxena V, Sadoqi M, Shao J. Degradation kinetics of indocyanine green in aqueous solution. J Pharm Sci 2003;92:2090–7.
[29] Shimizu S, Kamiike W, Hatanaka N, Yoshida Y, Tagawa K, Miyata M, et al. New method for measuring ICG Rmax with a clearance meter. World J Surg 1995;19:113–18.
[30] Holzer W, Mauerer M, Penzkofer A, Szeimies RM, Abels C, Landthaler M, et al. Photostability and thermal stability of indocyanine green. J Photochem Photobiol B 1998;47: 155–164.
[31] Vollrath A, Schubert S, Schubert US. Fluorescence imaging of cancer tissue based on metal-free polymeric nanoparticles - a review. J Mater Chem B 2013;1:1994–2007.
[32] Akbarzadeh A, Rezaei-Sadabady R, Davaran S, Joo SW, Zarghami N, Hanifehpour Y, et al. Liposome: classification, preparation, and applications. Nanoscale Res Lett 2013;8:102.
[33] Hadinoto K, Sundaresan A, Cheow WS. Lipid-polymer hybrid nanoparticles as a new generation therapeutic delivery platform: a review. Eur J Pharm Biopharm 2013;85:427–43.
[34] He X, Wang K, Cheng Z. *In vivo* near-infrared fluorescence imaging of cancer with nanoparticle-based probes. Wiley Interdiscip Rev Nanomed Nanobiotechnol 2010;2:349–66.
[35] Bartelmess J, Quinn SJ, Giordani S. Carbon nanomaterials: multi-functional agents for biomedical fluorescence and Raman imaging. Chem Soc Rev 2015;44:4672–98.
[36] Sano K, Ohashi M, Kanazaki K, Ding N, Deguchi J, Kanada Y, et al. *In vivo* photoacoustic imaging of cancer using indocyanine green-labeled monoclonal antibody targeting the epidermal growth factor receptor. Biochem Biophys Res Commun 2015;464:820–5.
[37] Xu HL, Shen BX, Lin MT, Tong MQ, Zheng YW, Jiang X, et al. Homing of ICG-loaded liposome inlaid with tumor cellular membrane to the homologous xenografts glioma eradicates the primary focus and prevents lung metastases through phototherapy. Biomater Sci 2018;6:2410–25.
[38] Liu Y, Yao T, Cai W, Yu S, Hong Y, Nguyen KT, et al. A biocompatible and near-infrared liposome for *in vivo* ultrasound-switchable fluorescence imaging. Adv Healthc Mater 2020;9:e1901457.
[39] Xue X, Fang T, Yin L, Jiang J, He Y, Dai Y, et al. Multistage delivery of CDs-DOX/ICG-loaded liposome for highly penetration and effective chemo-photothermal combination therapy. Drug Deliv 2018;25:1826–39.
[40] Hao Y, Chen Y, He X, Yu Y, Han R, Li Y, et al. Polymeric nanoparticles with ROS-responsive prodrug and platinum nanozyme for enhanced chemophotodynamic therapy of colon cancer. Adv Sci 2020;7:2001853 (Weinh).
[41] Wang J, Sun J, Hu W, Wang Y, Chou T, Zhang B, et al. A porous Au@Rh bimetallic core-shell nanostructure as an H_2O_2-driven oxygenerator to alleviate tumor hypoxia for simultaneous bimodal imaging and enhanced photodynamic therapy. Adv Mater 2020;32:e2001862.
[42] Liu C, Cao Y, Cheng Y, Wang D, Xu T, Su L, et al. An open source and reduce expenditure ROS generation strategy for chemodynamic/photodynamic synergistic therapy. Nat Commun 2020;11:1735.
[43] Chen H, Tian J, He W, Guo Z. H_2O_2-activatable and O_2-evolving nanoparticles for highly efficient and selective photodynamic therapy against hypoxic tumor cells. J Am Chem Soc 2015;137:1539–47.
[44] Hou H, Huang X, Wei G, Xu F, Wang Y, Zhou S. Fenton reaction-assisted photodynamic therapy for cancer with multifunctional magnetic nanoparticles. ACS Appl Mater Interfaces 2019;11:29579–92.
[45] Wang Y, Luo S, Wu Y, Tang P, Liu J, Liu Z, Shen S, et al. Highly penetrable and on-demand oxygen release with tumor activity composite nanosystem for photothermal/photodynamic synergetic therapy. ACS Nano 2020.
[46] Hu H, Yu L, Qian X, Chen Y, Chen B, Li Y. Chemoreactive Nanotherapeutics by Metal Peroxide Based Nanomedicine. Adv Sci 2020;8:2000494 (Weinh).
[47] He C, Zhang X, Xiang G. Nanoparticle facilitated delivery of peroxides for effective cancer treatments. Biomater Sci 2020;8:5574–82.
[48] Lin LS, Wang JF, Song J, Liu Y, Zhu G, Dai Y, et al. Cooperation of endogenous and exogenous reactive oxygen species induced by zinc peroxide nanoparticles to enhance oxidative stress-based cancer therapy. Theranostics 2019;9:7200–9.
[49] Kokate M, Garadkar K, Gole A. Zinc-oxide-silica-silver nanocomposite: unique one-pot synthesis and enhanced catalytic and anti-bacterial performance. J Colloid Interface Sci 2016;483:249–60.
[50] Li X, Jiang M, Zeng S, Liu H. Polydopamine coated multifunctional lanthanide theranostic agent for vascular malformation and tumor vessel imaging beyond 1500 nm and imaging-guided photothermal therapy. Theranostics 2019;9:3866–78.
[51] Huang J, Huang Y, Xue Z, Zeng S. Tumor microenvironment responsive hollow mesoporous Co9S8@MnO2-ICG/DOX

intelligent nanoplatform for synergistically enhanced tumor multimodal therapy. Biomaterials 2020;262:120346.
[52] Cheng X, He L, Xu J, Fang Q, Yang L, Xue Y, et al. Oxygen-producing catalase-based prodrug nanoparticles overcoming resistance in hypoxia-mediated chemo-photodynamic therapy. Acta Biomater 2020;112:234–49.
[53] Gholibegloo E, Karbasi A, Pourhajibagher M, Chiniforush N, Ramazani A, Akbari T, et al. Carnosine-graphene oxide conjugates decorated with hydroxyapatite as promising nanocarrier for ICG loading with enhanced antibacterial effects in photodynamic therapy against Streptococcus mutans. J Photochem Photobiol B 2018;181:14–22.
[54] Liu Y, Liu D, Zhu L, Gan Q, Le X. Temperature-dependent structure stability and *in vitro* release of chitosan-coated curcumin liposome. Food Res Int 2015;74:97–105.
[55] Giraudeau C, Moussaron A, Stallivieri A, Mordon S, Frochot C. Indocyanine green: photosensitizer or chromophore? Still a debate. Curr Med Chem 2014;21:1871–97.
[56] Lei Z, Zhang W, Li B, Guan G, Huang X, Peng X, et al. A full-spectrum-absorption from nickel sulphide nanoparticles for efficient NIR-II window photothermal therapy. Nanoscale 2019;11:20161–70.
[57] You Q, Zhang K, Liu J, Liu C, Wang H, Wang M, et al. Persistent regulation of tumor hypoxia microenvironment via a bioinspired Pt-based oxygen nanogenerator for multimodal imaging-guided synergistic phototherapy. Adv Sci 2020;7:1903341 (Weinh).
[58] Zhang Y, Guo C, Liu L, Xu J, Jiang H, Li D, et al. ZnO-based multifunctional nanocomposites to inhibit progression and metastasis of melanoma by eliciting antitumor immunity via immunogenic cell death. Theranostics 2020;10:11197–214 (Page 15). doi:10.7150/thno.44920.
[59] Lobatto ME, Calcagno C, Millon A, Senders ML, Fay F, Robson PM, et al. Atherosclerotic plaque targeting mechanism of long-circulating nanoparticles established by multimodal imaging. ACS Nano 2015;9:1837–47.
[60] Pastorino F, Brignole C, Marimpietri D, Cilli M, Gambini C, Ribatti D, et al. Vascular damage and anti-angiogenic effects of tumor vessel-targeted liposomal chemotherapy. Cancer Res 2003;63:7400–9.
[61] Shao L, Li Y, Huang F, Wang X, Lu J, Jia F, et al. Complementary autophagy inhibition and glucose metabolism with rattle-structured polydopamine@mesoporous silica nanoparticles for augmented low-temperature photothermal therapy and *in vivo* photoacoustic imaging. Theranostics 2020;10:7273–86.
[62] Tang YA, Chen YF, Bao Y, Mahara S, Yatim S, Oguz G, et al. Hypoxic tumor microenvironment activates GLI2 via HIF-1alpha and TGF-beta2 to promote chemoresistance in colorectal cancer. Proc Natl Acad Sci U S A 2018;115:E5990–9.
[63] Wang M, Zhao X, Zhu D, Liu T, Liang X, Liu F, et al. HIF-1alpha promoted vasculogenic mimicry formation in hepatocellular carcinoma through LOXL2 up-regulation in hypoxic tumor microenvironment. J Exp Clin Cancer Res 2017;6:60.